AGU PUBLICATIONS

JGR

Journal of Geophysical Research: Space Physics

RESEARCH ARTICLE
10.1002/2013JA019402

Key Points:
- This paper studies ionospheric responses to solar wind pressure enhancements
- The ionosphere forms complicated transient shapes when solar wind varies
- The escape fluxes depend on both simultaneous and earlier solar wind conditions

Correspondence to:
Y. J. Ma,
yingjuan@igpp.ucla.edu

Citation:
Ma, Y. J., X. Fang, A. F. Nagy, C. T. Russell, and G. Toth (2014), Martian ionospheric responses to dynamic pressure enhancements in the solar wind, *J. Geophys. Res. Space Physics*, *119*, 1272–1286, doi:10.1002/2013JA019402.

Received 3 SEP 2013
Accepted 10 JAN 2014
Accepted article online 3 JAN 2014
Published online 18 FEB 2014

Martian ionospheric responses to dynamic pressure enhancements in the solar wind

Y. J. Ma[1], X. Fang[2], A. F. Nagy[3], C. T. Russell[1], and Gabor Toth[3]

[1]Institute of Geophysics and Planetary Physics, UCLA, Los Angeles, California, USA, [2]Laboratory for Atmospheric and Space Physics, University of Colorado Boulder, Boulder, Colorado, USA, [3]Department of Atmospheric, Oceanic and Space Sciences, University of Michigan, Ann Arbor, Michigan, USA

Abstract As a weakly magnetized planet, Mars ionosphere/atmosphere interacts directly with the shocked solar wind plasma flow. Even though many numerical studies have been successful in reproducing numerous features of the interaction process, these earlier studies focused mainly on interaction under steady solar wind conditions. Recent observations suggest that plasma escape fluxes are significantly enhanced in response to solar wind dynamic pressure pulses. In this study, we focus on the response of the ionosphere to pressure enhancements in the solar wind. Through modeling of two idealized events using a magnetohydrodynamics model, we find that the upper ionosphere of Mars responds almost instantaneously to solar wind pressure enhancements, while the collision dominated lower ionosphere (below ~150 km) does not have noticeable changes in density. We also find that ionospheric perturbations in density, magnetic field, and velocity can last more than an hour after the solar wind returns to the quiet conditions. The topside ionosphere forms complicated transient shapes in response, which may explain unexpected ionospheric behaviors in recent observations. We also find that ionospheric escape fluxes do not correlate directly with simultaneous solar wind dynamic pressure. Rather, their intensities also depend on the earlier solar wind conditions. It takes a few hours for the ionospheric/atmospheric system to reach a new quasi-equilibrium state.

1. Introduction

Mars does not currently possess a significant intrinsic magnetic field [*Acuna et al.*, 1998]; thus, its ionosphere/atmosphere interacts directly with the shocked solar wind plasma flow. The solar wind contains small and short time scale structures ubiquitously as well as large and long time scale structures such as occasional interplanetary coronal mass ejections (ICMEs) and corotating interaction regions (CIRs). However, there is little understanding of the ionospheric responses to solar wind variations due to the lack of coordinated observations of both upstream solar wind conditions and simultaneous plasma properties in the Martian ionosphere.

Even though it has not been possible to relate instantaneous responses of the plasmas in the ionosphere to variations in the solar wind, statistical studies have been performed to examine how total escape fluxes vary with different solar wind conditions [*Lundin et al.*, 2008; *Nilsson et al.*, 2010; *Edberg et al.*, 2010]. All of the studies found a positive correlation between ion escape rates and upstream solar wind dynamic pressure inferred from the peak magnetic field strength in the magnetic pileup region. Some individual large solar energetic particle and CIR events were also studied based on limited observations [*Futaana et al.*, 2008; *Dubinin et al.*, 2009] and the results indicated approximately 1 order of magnitude enhancements in the heavy ion outflow flux from the Martian atmosphere during the events. A recent study by *Opgenoorth et al.* [2013] examined a number of isolated CIR and ICME events in March and April 2010 and found that the magnetosphere and ionosphere of Mars can become considerably compressed by enhanced solar wind dynamic pressures.

Many numerical models have been applied to Mars to understand the solar wind interaction with its atmosphere/ionosphere system [*Ma et al.*, 2002, 2004; *Modolo et al*, 2006; *Harnett and Winglee*, 2006, 2007; *Fang et al.*, 2008; *Harnett*, 2009; *Boesswetter et al.*, 2010; *Kallio et al.*, 2009, 2010; *Najib et al.*, 2011; *Dieval et al.*, 2012; *Brecht and Ledvina*, 2012]. Those models used nominal steady state solar wind conditions and were successful in reproducing many observational features of the interaction process. There are also some studies that focused on the interactions under extreme solar wind conditions, in current or early Mars conditions. *Ma and Nagy* [2007], using steady solar wind conditions, found that during extreme space weather events, the total ion escape fluxes could be about 2 orders of magnitude larger than those at quiet times. In addition,

Terada et al. [2009] studied ion escape rates under extreme early Mars conditions and found that when the solar EUV flux is 100 times higher than today and the solar wind is 300 times denser, the O^+ loss rate could reach 1.5×10^{28} ions/s, which is about 10^4 times greater than today's value. Very recently, a global numerical study by *Fang et al*. [2013] showed that pickup ion precipitation could be considerably intensified under the impact of extreme solar wind conditions, resulting in dramatic neutral temperature enhancement and significant neutral composition and wind changes. However, little is known about how the ionosphere responds to time-varying solar wind conditions or how long it takes the ionospheric system to reach a new equilibrium state.

By examining electron density profiles from the Mars Express Radio Science Experiment, *Withers et al*. [2012] found that the vertical structure of the dayside ionosphere of Mars was more variable and complex than expected from a simple Chapman model. For example, the top of the ionosphere has been observed to vary from below 250 km to above 650 km; the topside ionosphere can be described by a single scale height or two/three regions with distinct scale heights, where those scale heights range between tens and hundreds of kilometers; the main layer of the ionosphere can have different shapes from a typical Chapman prediction. They also found that occasionally a broad increase appeared in electron density at 160–180 km, and at other times, a narrow increase in electron density in strongly magnetized regions. Many of these observed features cannot be explained by a simple ionospheric model. Here we propose that many of the above structures are likely caused by changes in the solar wind plasma and associated interplanetary magnetic field. To test this idea, we use a time-dependent global magnetohydrodynamics (MHD) model to study how the ionosphere responds to discontinuities in solar wind density and velocity and also estimate for the first time the response time of the Martian ionospheric system to external force changes. We will briefly describe the model that is used for the study in section 2. The model results are presented in section 3. A summary is given in section 4.

2. Numerical Model

We use a multispecies single-fluid MHD model based on the Block Adaptive Tree Solar-Wind Roe Upwind Scheme code [*Powell et al*., 1999; *Toth et al*., 2012] to study ionospheric response to abrupt variations in the solar wind. The model is described in detail by *Ma et al*. [2004], except that the solar wind electron impact ionization has been considered and a new spherical grid has been implemented. To capture small-scale changes in the Martian ionosphere, the radial resolution is further improved to about 5 km from 100 to 600 km. About one third of the total computational grids are inside 600 km altitude region. Above 600 km, the radial resolution is gradually degraded to 630 km near the downstream outer boundary. The angular resolution is 3° in both latitudinal and longitudinal directions. The number of cells is 2.1 million in total. In this paper, we chose to use the multispecies single-fluid model because a multifluid model [e.g., *Najib et al*., 2011] is too computationally expensive for the time-dependent case.

The multispecies single-fluid MHD model [*Ma et al*., 2004] includes four continuity equations to track the mass densities of the proton and three major ions in the Martian ionosphere: O_2^+, O^+, and CO_2^+. All the ion species are assumed to share the same velocity and temperature. The Mars-solar wind interaction is self-consistently calculated in the model by including the effects of the crustal magnetic field, ion-neutral collisions, and major chemical reactions. The neutral densities of CO_2, O, and H are assumed to be spherically symmetric, and the profiles are the same as used for solar maximum condition in *Ma et al*. [2004]. We consider photoionization, electron impact ionization, charge exchange, and recombination reactions in the calculation. The photoionization rates are dependent on the solar zenith angle with optical depth considered [*Schunk and Nagy*, 2009].

Simulations are performed in the Mars centered coordinate system: The X axis points from Mars toward the Sun, the Z axis is perpendicular to the X axis and parallel to the projection of the planet rotation axis on a plane perpendicular to the X axis, and the Y axis completes the right-handed coordinate system. The computational domain used in the calculation is the same as in *Ma et al*. [2004], which is defined by $-24\ R_M < X < 8\ R_M$, $-16\ R_M < Y, Z < 16\ R_M$, where R_M is the radius of Mars (3396 km).

The inner boundary is set at 100 km altitude, assuming ion densities are in photochemical equilibrium. Plasma temperature (T_P) is assumed to be twice the neutral temperature and pressure is set accordingly at the inner boundary. The magnetic field is set to be the same as the crustal magnetic field. We used the 60-order harmonic

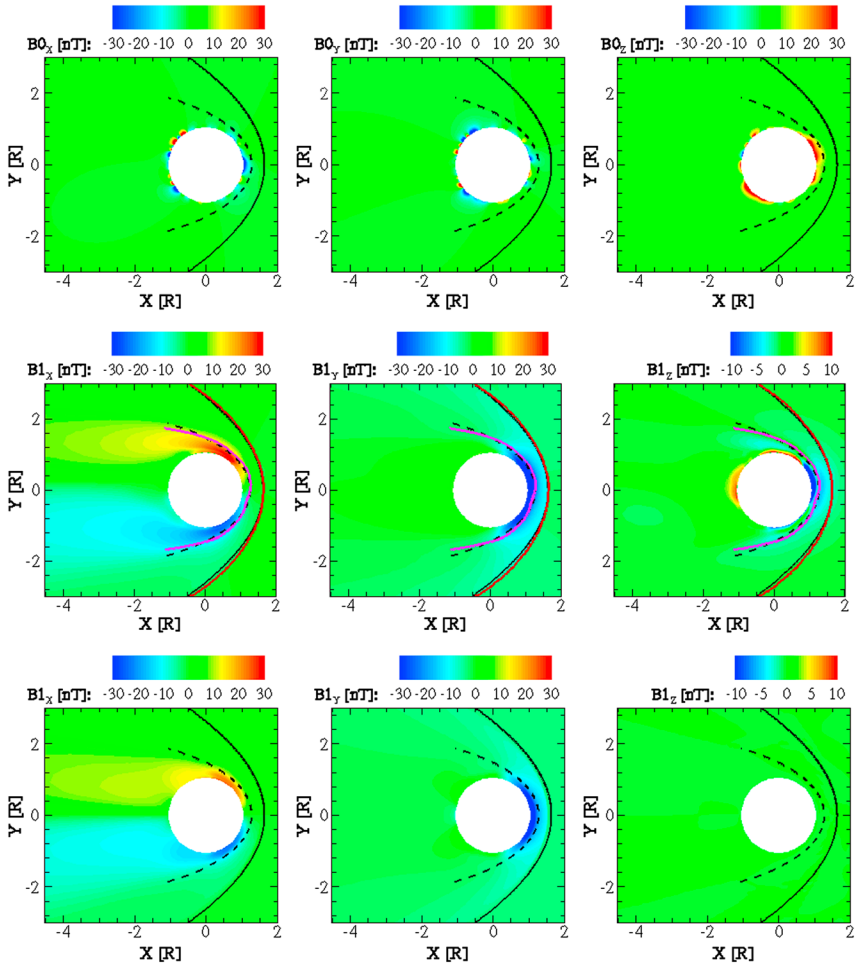

Figure 1. Magnetic field contour plots in the *XY* plane. (top) Components of the crustal field used in the model. (middle) Components of the induced magnetic field at steady state, while (bottom) the induced magnetic field for an ideal case with no crustal field included. The observed bow shock and MPB are represented by the black solid line and the black dashed line, respectively [*Vignes et al.*, 2000]. In Figure 1 (middle), the model-calculated BS and MPB locations are shown with the red line and purple line, respectively.

expansion of *Arkani-Hamed* [2001] to estimate the crustal field. In the calculation, the subsolar position is set to be at 180° longitude, which corresponds to a relatively strong crustal field source. Note that in the simulation presented in the paper, the strong crustal field region (180°W longitude) is facing toward the Sun and the rotation of the planet is neglected.

Using the model, we investigate two idealized solar wind dynamic pressure enhancement events with time-varying solar wind conditions. In Event 1 the density is enhanced with all the other input parameters unchanged, and in Event 2 the velocity is increased. The perturbation of the solar wind propagates into the simulation domain from the upstream outer boundary that is located at 8 R_M. We first run the code using constant quiet solar wind conditions for 2 h to reach a steady state, which serves as our starting point for both events. The solar wind conditions for quiet time are set as follows: $n_{sw} = 4\ \mathrm{cm}^{-3}$, $U = -400$ km/s, $B_Y = -3$ nT, and plasma temperature $T_P = 3.5 \times 10^5$ K. This set of parameters corresponds to a dynamic pressure of about 1.1 nPa and magnetosonic Mach number of $M_f = 5.7$. The disturbed solar wind then starts to propagate into the computational domain from the upstream outer boundary at 2:00 UT and lasts for 30 min, followed by additional 2.5 h quiet solar wind conditions. These are two idealized events of dynamic pressure pulses. In reality, the density, velocity, and magnetic field could all vary. However, the changes of these parameters are mixed, making it challenging to distinguish causes and consequences. In this sense, simple events are more useful in probing the physical processes in the Mars-solar wind interaction. The simulation results of both events are presented in the next section.

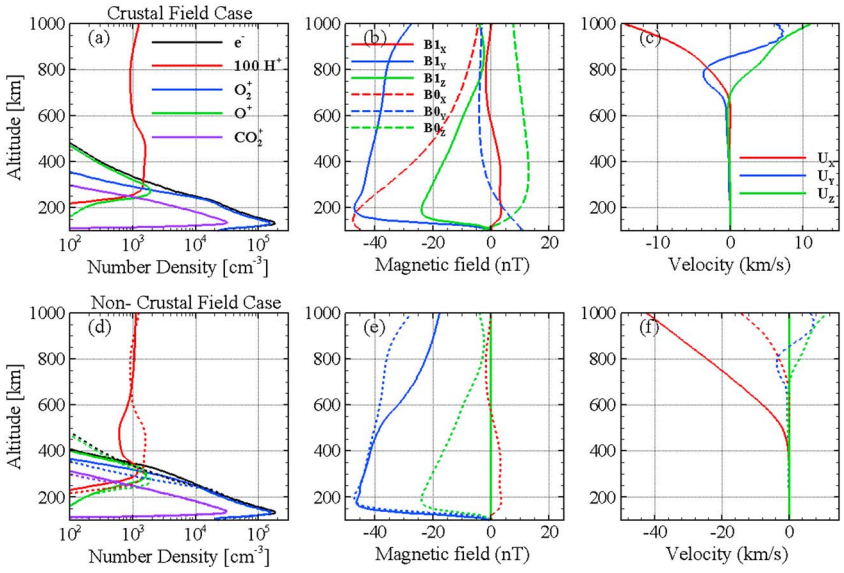

Figure 2. Profiles of various plasma properties along the subsolar line at steady state. (a–c) For the case with the crustal field and (d–f) for the noncrustal field case. Figures 2a and 2d show altitude profiles of number densities of different ion species and electrons, and Figures 2b and 2e and 2c and 2f show altitude profiles of magnetic field and velocity components, respectively. We also overplotted the results for the case with the crustal field in dashed lines in Figures 2d–2f for comparison.

3. Simulation Results

3.1. Steady State at Quiet Time

Before we show the ionospheric changes in response to the solar wind dynamic pressure enhancements, we first examine the steady state behaviors when the incoming solar wind is quiet. The results at steady state are similar to what has been presented in *Ma et al*. [2004]. In order to better understand the role of the crustal field at low altitudes in affecting the near-Mars space environment, here we compare two cases for the quiet solar wind conditions: one with the presence of the crustal field and the other without.

Figure 1 shows the crustal field and induced magnetic field distributions in the *XY* plane for two cases (steady state case and a noncrustal field case for comparison). We use the subscripts 0 and 1 to denote the crustal and induced fields, respectively. As seen from the plot, even though the crustal field is only strong in limited regions close to the planet, the induced fields for the two cases differ notably even in the regions outside the magnetic pileup boundary (MPB). The induced field has similar draping patterns in the dayside for the two cases, but the induced field is significantly enhanced and extends to higher altitudes in the case with the crustal field compared with the no-crustal-field case. Also a dawn-dusk asymmetry is shown in the tail region for the $B1_X$ component in the crustal field case. The $B1_Z$ component is nearly zero in the *XY* plane in the case with no crustal field, while there is a finite value of $B1_Z$ due to the existence of the crustal field. But the induced $B1_Z$ component is generally weaker compared to the other two induced field components as well as the *Z* component of the crustal field $B0_Z$. This comparison shows that the existence of the crustal field significantly alters the region and values of the induced field.

In Figure 1 (middle), the model-calculated bow shock (BS) and MPB locations are plotted with red lines and purple lines, respectively. Here the MPB is approximated by the location where the magnetic pressure is balanced with the solar wind thermal pressure. The BS is approximated by the region of fast magnetosonic Mach number of 2.5. The statically averaged boundary locations by *Vignes et al*. [2000] are superposed for reference. As shown in the plot, the calculated BS and MPB locations agree well with observations.

We show in Figure 2 plasma properties (plasma number densities, magnetic field, and bulk velocity) along the subsolar line from 100 km to 1000 km altitude for the steady state case with crustal field (Figures 2a–2c) together with the case that contains no crustal field (Figures 2d–2f) for comparison.

Figures 2a and 2d compare the number density profiles of electrons and the four ion species for the two cases. The ion density profiles are almost identical at lower altitude but start to deviate above 250 km altitude as shown in Figure 2d. For the crustal field case, the subsolar ionospheric upper boundary is located at

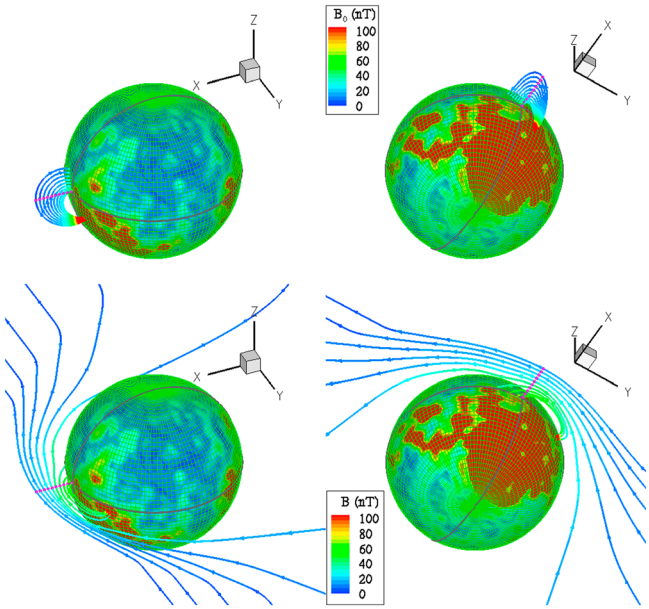

Figure 3. The geometry of magnetic field lines tracing through selected subsolar points. The field lines are generated through 10 equally spaced subsolar points from 1.05 R_M to 1.5 R_M. (top) The crustal magnetic field lines from two different points of view and (bottom) the total magnetic field lines (crustal field + induced field) at 2:00 UT steady state. The arrows show field line directions, and the colors indicate the strength of the crustal (Figure 3, top) or total magnetic field (Figure 3, bottom). The sphere shows the inner boundary of the simulation domain; the mesh on the sphere shows grid used in the simulation.

roughly 480 km altitude, assuming that the top of the ionosphere is roughly where the electron number density is equal to 100 cm^{-3}. The ionospheric upper boundary used in the paper is not strictly a plasma boundary; rather, it is used as an indication of roughly how far the ionosphere extends. We use this criterion instead of the pressure balance criterion to approximate the location of the upper boundary of the ionosphere (normally referred to as ionopause) location because the ionosphere peak pressure (~0.8 nP) is smaller than the upstream solar wind dynamic pressure. This is somewhat higher than the observed ionopause location ~ 300 km [*Withers et al*., 2012]. The reason for the higher ionospheric upper boundary is twofold: (1) the relatively strong crustal field in the region and (2) the calculation is based on solar maximum conditions. For the noncrustal field case, the ionosphere top boundary is located at about 400 km height along the subsolar line, as shown in Figure 2d. In the case with the crustal field, the magnetic pressure from the crustal field also contributes to standing off the shocked solar wind. Therefore, the upper boundary of the ionosphere for the crustal field case is usually farther away as compared with the noncrustal field case. It is expected that the upper boundary is located at lower altitudes during solar minimum conditions because of the weaker ionosphere due to the lower photoionization frequency. In both cases, the upper boundary locations are within the range of the observations by *Withers et al*. [2012].

Figures 2b and 2e show that the induced fields are similar for the two cases at low altitudes for the $B1_Y$ component. The induced field drops to zero at 100 km because we force the magnetic field at the inner boundary to be the same as the local crustal field. The crustal field along the subsolar line peaks at 150 km with a value of 46 nT, which is dominated by the *X* component. This crustal field is about the same order as the peak value of the induced field, and this explains why the ionospheric upper boundary is higher for the crustal field case. Also note that the induced field has the opposite sign, as compared with the crustal field for both *X* and *Z* components below 600 km altitude along the subsolar line. However, the induced magnetic field usually has complicated relation with the crustal field as indicated by Figure 1.

As shown in Figures 2c and 2f, the shocked solar wind flow continues to move toward the planet at around 1000 km altitude for both cases, but the flow speed is much larger for the noncrustal field case (note the scales are different for the two panels). The flow speed gradually slows down as the plasma moves closer to the planet, and the dynamic energy is converted to magnetic energy for both cases but drops much faster along the subsolar line for the crustal field case. For the noncrustal field case, the solar wind penetrates deeper not only

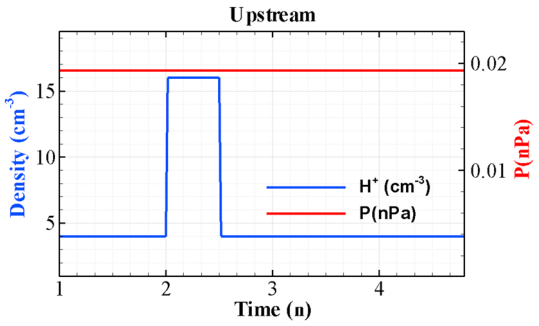

Figure 4. Upstream solar wind density and thermal pressure profiles for Event 1. The quiet time solar wind density is 4 cm^{-3} and increases to 4 times denser for 30 min. A step function is used as an ideal event of the pressure enhancement.

along the subsolar line but also generally in the ram side. Also for the noncrustal field case, the plasma flow along the subsolar line only moves along the X direction, while for the crustal field case, there are significant flows along the Y and Z directions.

Figure 3 shows the geometry of magnetic field lines passing through selected subsolar points for the crustal field case. The field lines are traced through 10 equally spaced subsolar points from $X = 1.05\ R_M$ to $1.5\ R_M$ based on either the crustal magnetic field (Figure 3, top) or the total magnetic field (Figure 3, bottom). Figure 3 (top) show that these subsolar points are all on closed crustal field lines. All of these field lines come out from a strong crustal field region located in the Southern Hemisphere and enter into a relatively weak crustal field region slightly north of the equator. Due to the solar wind magnetic field draping and compression, the resulting magnetic field lines that pass through these spatial points are significantly altered in both shape and orientation (see Figure 3 (bottom)). The magnetic field varies from a closed to an open configuration above $1.25\ R_M$. Although the total field line at low altitudes is still closed, its direction changes from mainly south-north to east-west due to the contribution of the induced magnetic field, whose direction is mainly controlled by the interplanetary magnetic field ($-Y$ direction). The feet of these closed field lines move closer to the equator, although they still come out of a strong crustal field region and enter a relatively weak crustal field region.

It is clear that the crustal field has significant influence on the interaction between Mars and the solar wind. It is expected that when including the rotation of the planet (and thus the crustal field), the interaction would be more complicated. The test particle simulations by *Fang et al*. [2010a, 2010b] using the MHD model-calculated background fields show that the inclusion of the crustal field local time effects also significantly changes the behavior of how pickup ions escape to space or return to the planet. For simplicity, we fix the strong crustal field on the dayside during the pass of solar wind dynamic pressure enhancements for the simulations shown below. However, Figures 1–3 clearly suggest that the rotation of the crustal field with the planet needs to be taken into account in future studies.

3.2. Event 1: Solar Wind Density Enhancement Event

We first examine the results of the Mars interaction with a solar wind density enhancement event (i.e., contact discontinuity). The solar wind density varies with time, as shown in Figure 4. The solar wind plasma condition is assumed to be quiet for the first 2 h to ensure a steady state, then the density jumps from 4 cm^{-3} to 16 cm^{-3}. At the same time, the thermal temperature is decreased to one fourth of the quiet time value so that the solar wind thermal pressure is balanced across the density discontinuity. We assume that the density enhancement lasts for 30 min and then drops back to the normal level. During the event, the solar wind velocity and magnetic field are kept constant.

Figure 5 shows snapshots of various plasma properties including ion densities, the induced magnetic field, and plasma velocity components along the subsolar line at different simulation times in a format similar to Figure 2. The steady state solution is shown in dashed lines for reference, which is identical to the results at 2:00 UT as shown in Figures 5a1–5c1. At 2:00 UT, the disturbed solar wind crosses the outer boundary at $X = -8\ R_M$ and enters the simulation domain. For a constant 400 km/s flow speed, it takes roughly 1 min for the solar wind to propagate from 8 R_M upstream to Mars when neglecting the slowing down of the flow. Inside the bow shock, the plasma flow is subsonic, but the information of the density pulse propagates at the fast magnetosonic speed. At 2:01:30 UT, the plasma properties in the upper ionosphere are already significantly disturbed. The top boundary of the ionosphere moves slightly downward. A new peak forms at around 180–200 km altitude in addition to the main peak. At the same time, both the induced field and plasma flow velocity are greatly enhanced (Figures 5b2 and 5c2). At 1000 km, the antisunward plasma velocity increases from 15 km/s by more than a factor of 3 due to the increase of the solar wind dynamic pressure. The vertical profile of the induced magnetic field also changes, forming a broad peak at high altitudes and a narrow peak

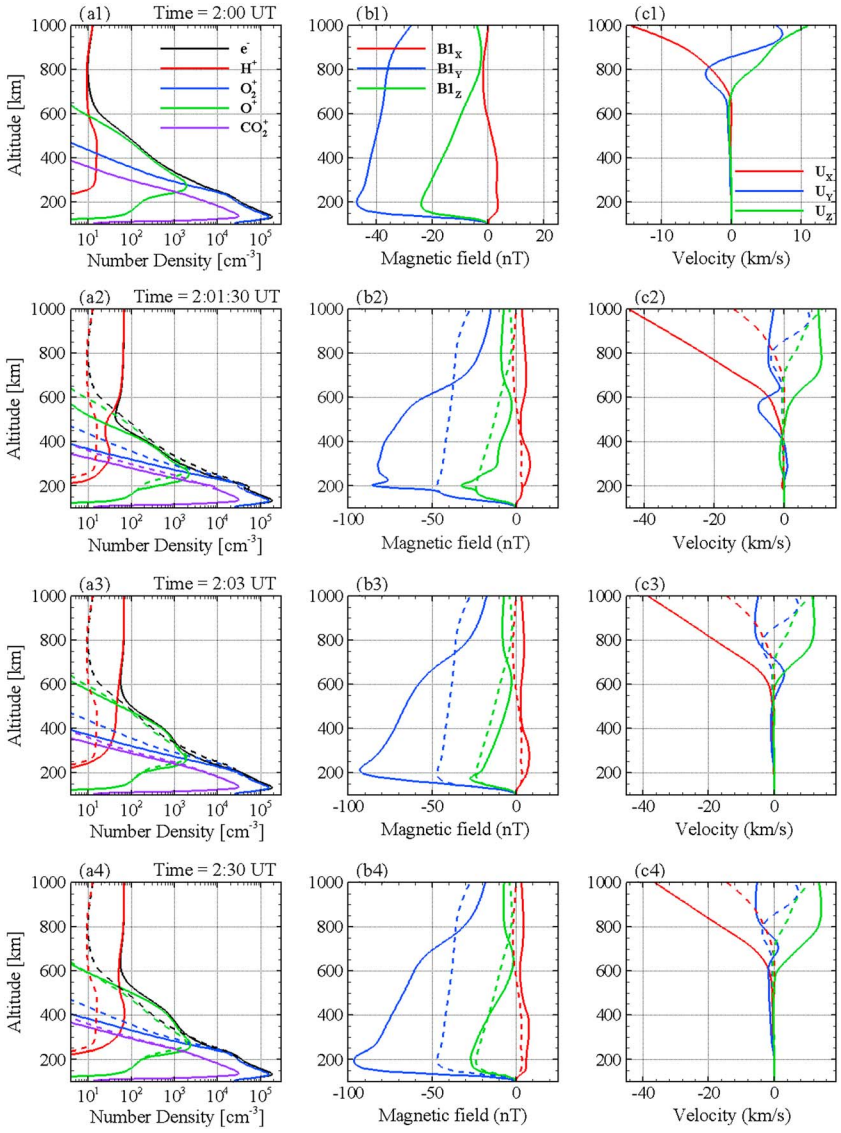

Figure 5. Snapshots of various plasma properties along the subsolar line at different simulation times. (a1–a8) Altitude profiles of number densities of different ion species and electrons, and (b1–b8 and c1–c8) altitude profiles of magnetic field and velocity components, respectively.

at around 200 km. The magnitude of the induced field is nearly doubled from 45 nT to 87 nT at around 200 km altitude. These profiles demonstrate that the ionosphere responds to the solar wind density variation almost instantaneously. It is worth noting that the additional peak in electron density seems only a transient feature as it disappears very shortly as shown in Figure 5a3. This panel also shows that the density of O^+ is enhanced at 2:03 UT between 300 km and 500 km altitude. Above 300 km, the density of H^+ is also greatly enhanced compared with the steady state condition, which could potentially increases the charge exchange reaction rates between the H^+ and oxygen atoms and contributes to the enhancement of O^+. However, in this region, photoionization is still the dominant source of O^+, and its rate is at least 6 times larger than that of the charge exchange reaction. Thus, charge exchange is unlikely the main cause of the enhancement. In fact, in this region, the plasma still moves downward with a finite speed ~ 0.5 km/s, which compresses the ionosphere and is the main cause of the enhancement of the O^+ density. The induced field increases to as much as ~ 96 nT with a completely different shape as compared with that at quiet times. After 2:03 UT until 2:30 UT, before the solar wind density returns to the normal state, the ionospheric density profiles together with the magnetic field and flow velocity all slowly vary to reach a new quasi steady state. Even though the upper boundary of the ionosphere does not move much during the compression, the electron density profile significantly altered its shape

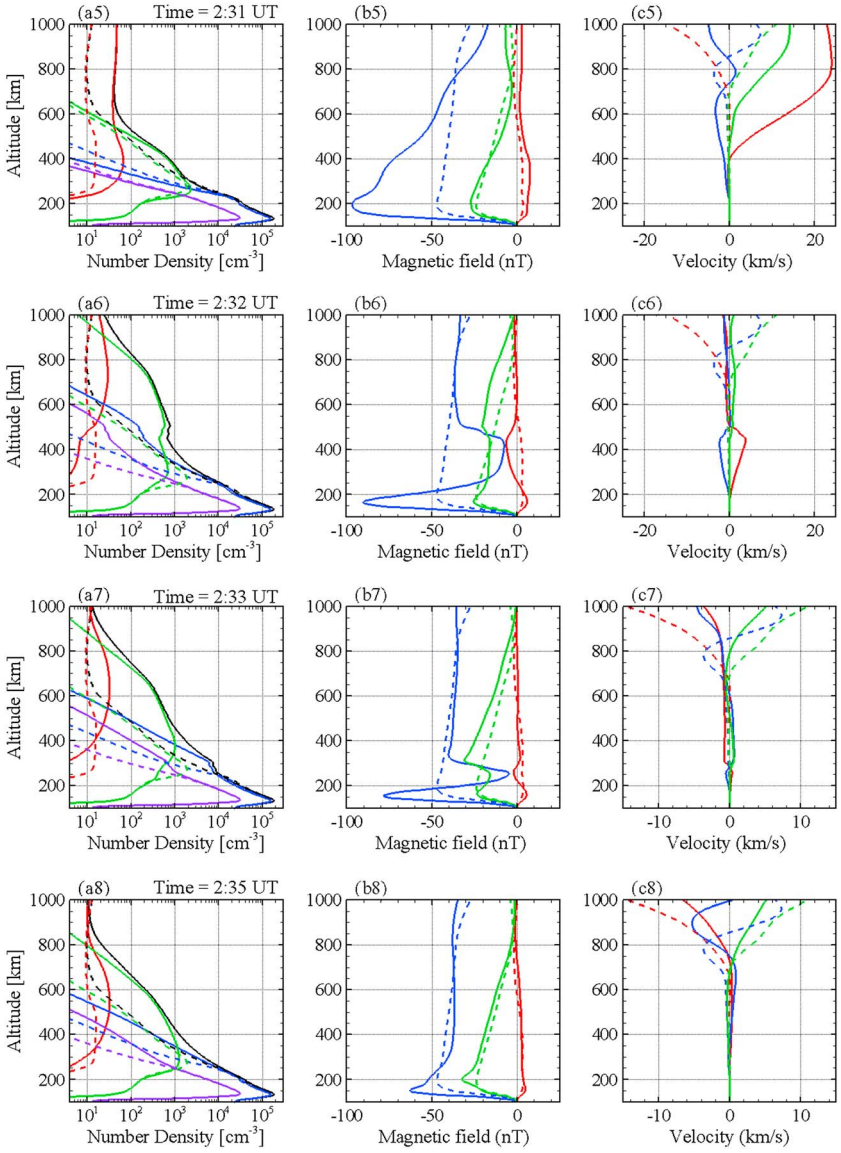

Figure 5. (continued)

and showed distinct scale heights around different altitude region. This demonstrated that the solar wind dynamic pressure has important influence on plasma properties in the upper ionosphere.

At 2:31 UT, only 1 min after the upstream solar wind density recovers, the plasma flow has already changed its direction to move upward with a speed of 20 km/s (see Figure 5c5). The system was previously in a roughly balanced state, where the solar wind dynamic pressure is balanced by the ionospheric thermal pressure and magnetic pressure. Due to the sudden drop of the solar wind pressure, the forces pushing outward overcome the inward forces, moving the plasma in the ionosphere upward. As a result, at 2:32 UT (2 min after the passage of the solar wind dynamic pressure pulse), the topside ionosphere extends from 480 km to 830 km altitude (Figure 5a6), far beyond the location of the top of the ionosphere during quiet time. An interesting feature of the magnetic field is shown in Figure 5b6, where the magnetic field has a broad dip (~200 km wide) near 400 km altitude. However, this also appears to be a transient structure, as the dip shrinks (Figure 5b7) and disappears at 2:35 UT (Figure 5b8). The ionosphere along the subsolar line has already started to move down at 2:33 UT. After 2:36 UT, the ionosphere only varies slowly, with the top boundary of the ionosphere gradually dropping back to its original location. The new quasi steady state is reached at about the end of the simulation, which is at 5:00 UT.

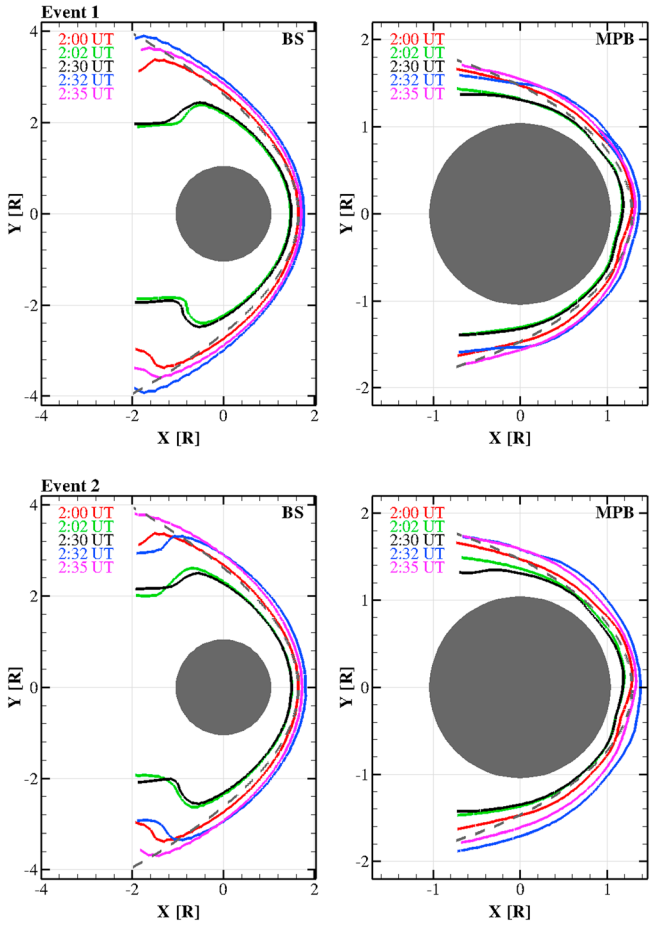

Figure 6. (left) Bow shock and (right) MPB locations in the *XY* plane at different times for (top) Event 1 and (bottom) Event 2. The observed BS and MPB boundaries from *Vignes et al.* [2000] are plotted in grey dashed lines for reference.

The top two panels of Figure 6 show the variation of the interaction boundaries during the event at several different times. Figure 6 (left and right) shows the bow shock locations and MPB locations in the *XY* plane, respectively. Here the MPB and BS locations are determined using the same method as discussed earlier in the paper. The locations of the MPB and BS in the equatorial plane at quiet time (2:00 UT) agree well with the results from the statistical study by *Vignes et al.* [2000] as shown earlier in Figure 1. Shortly after the density enhancement propagates to Mars, both boundaries quickly move inward to adjust to the new solar wind condition as marked by the green lines (2:02 UT), indicating that the magnetosphere is considerably compressed by the solar wind dynamic pressure enhancement, consistent with the findings of *Opgenoorth et al.* [2013]. From 2:02 UT to 2:30 UT, the boundaries seldom move, indicating that the response of the plasma boundaries to the solar wind pressure enhancement is almost instantaneous. Two minutes after the density drop of the solar wind, both BS and MPB expand outward significantly, as shown by the blue lines. The two boundaries then gradually shrink as time goes by. It takes about 10 min for the two boundaries to reach their quasi steady state location. This shows that depending on the nature of the solar wind perturbation, the response time of the plasma boundaries could vary significantly.

Figure 7 (top) shows variations of the ionospheric top boundary locations in the *XY* plane during the events. As discussed earlier in the paper, the upper boundary locations are estimated by the region of an electron density of 100 cm^{-3}. The calculated boundaries at different times are plotted in the altitude-local time map. The crustal field strength is overplotted in the figure in gray shadings. The purple dashed line represents the upper boundary from the noncrustal field case for comparison. When there is no crustal field, the ionospheric upper boundary is smooth, and its location depends mainly on local time. The inclusion of crustal field significantly changes the shape of ionospheric upper boundary even at steady state, as shown with the red line;

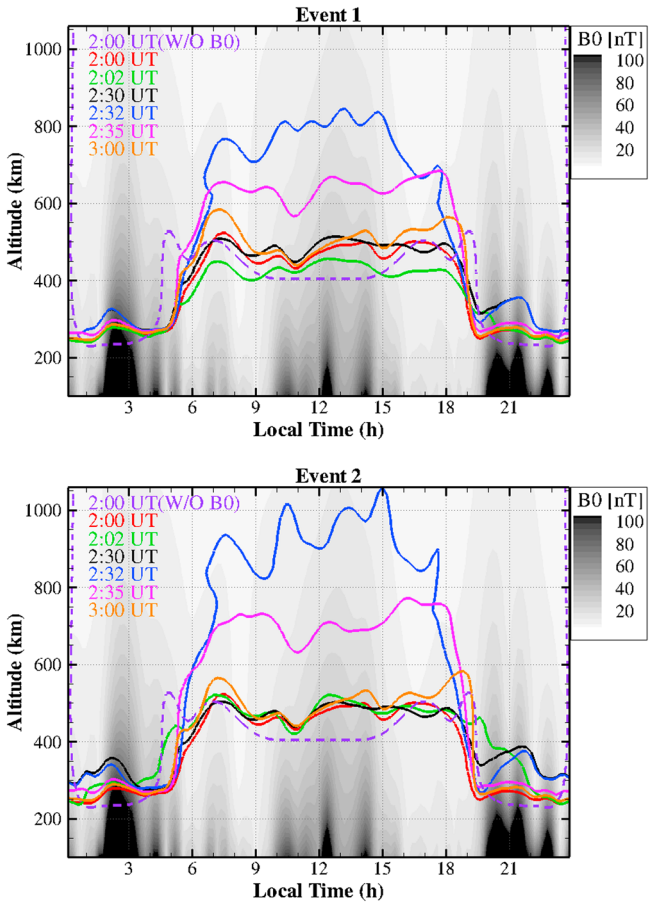

Figure 7. Variations of the top boundary of the ionosphere in the XY plane for (top) Event 1 and (bottom) Event 2. The top boundaries of the ionosphere are estimated by the contour line of electron density equals to 100 cm^{-3}. The background color indicates the crustal field strength. The purple dashed line denotes the ionosphere top boundary for the noncrustal field case.

the ionosphere usually extends to higher altitude near strong crustal field regions. At 2:02 UT, 2 min after the start of the solar wind density enhancement, the boundary moves closer to the planet, even in the regions away from the subsolar point, as shown by the green line. The ionosphere then expands outward as a result of the increase of plasma temperature due to enhanced solar wind heating. Only 2 min after the solar wind density/dynamic pressure drop, the boundary moves drastically upward. The ionosphere top boundary near the subsolar point is lifted to around 800 km. After that, boundary slowly moves back toward the planet in the dayside region. In contrast, the ionosphere near the terminator keeps expanding, indicating that those ions that are picked up by the solar wind in the dayside region move antisunward to help refill the ionosphere there. Even at 3:00 UT, the ionospheric upper boundary is still located slightly higher than that at the quiet time, indicating that the ionosphere has not completely returned to its equilibrium state yet.

The solid lines in Figure 8 show the variation of integrated ion escape fluxes with time during the density enhancement event. The upstream solar wind dynamic pressure is also shown by the black dashed line. The escaping fluxes are estimated by integrating over $R = 6\ R_M$ sphere of the plasma flux in radial direction (plasma density times the radial velocity). The integral fluxes are nearly constant once the radius exceeds 3 R_M. The main escape ion species is O^+ for the entire duration. The fluxes are constant before the solar wind density enhancement at 2:00 UT. During quiet times, O^+ flux is 4.6×10^{24}/s, about 7.3 times larger than the O_2^+ flux. Right after the solar wind density increases, the O^+ flux slightly decreases. This is mainly due to the compression of the dayside ionosphere enforced by the enhancement of the dynamic pressure of the solar wind. It is followed by an abrupt increase of the O^+ flux reaching nearly twice its quiet time value only 3 min after 2:00 UT. The O^+ flux then gradually increases until 2:30 UT to 1.43×10^{25}/s, about 3.1 times the quiet time flux value. When the solar wind density drops at 2:30 UT, the solar wind dynamic pressure decreases and the

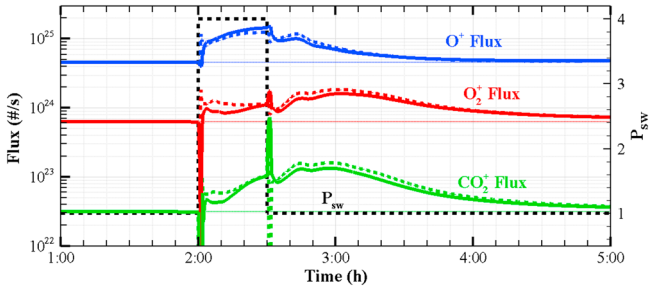

Figure 8. Variation of ion escape fluxes with time during Event 1 (solid lines) and Event 2 (dashed lines). It is overplotted with upstream solar wind dynamic pressure in black dashed line.

escape flux of O^+ also decreases sharply as expected. However, an interesting but somewhat unexpected increase in the O^+ escape flux takes place between 2:34 UT and 2:44 UT. This is because the ionosphere expands rapidly from 550 km to 800 km altitude (as seen in Figure 7) in response to the decreasing of the solar wind pressure, and more atmospheric atoms are liable to solar wind pickup loss, which results in an increased escape rate. After 2:44 UT, the O^+ flux starts to drop again gradually. At 4:00 UT, about 1.5 h after the solar wind density returns to its quiet time value, the O^+ flux is still 10% above its normal value. The responses of O_2^+ and CO_2^+ have similar trends with different relative scales except at 2:30 UT, when the fluxes of both molecular heavy ions have a considerable increase due to the different chemical reactions that are involved. Also, the recovery time for the two heavy ions is even longer than O^+. At 4:00 UT, both O_2^+ and CO_2^+ are still more than 50% above their normal values. In summary, the most important message from the escape fluxes variation plot is the fast initial response and the long-time recovery of the ionosphere system.

3.3. Event 2: Solar Wind Velocity Enhancement Event

We run another solar wind dynamic pressure pulse event (Event 2), in which the solar wind density is kept constant, but the flow speed is doubled for 30 min and then dropped back. This is a more complicated event than the first one, because such a discontinuity cannot be stable. As the perturbations propagate into the computational domain, it evolves quickly into a shock where velocity jumps up and into a rarefaction wave where it jumps back. As shown in Figure 9, at 2 R_M upstream, the perturbations in density are very short in time scale. The density enhancement near 2:30 UT lasts for less than a minute, and the density decrease near 2:30 UT is less than 2 min.

Figure 10 shows a similar plot to Figure 5 for the velocity enhancement event. Similar to the density enhancement event at 2:00 UT, the perturbation of the solar wind is just crossing the outer boundary at $X = -8\ R_M$ and entering the simulation domain. However, since the solar wind speed doubles in this event, the propagation time is much shorter from the upstream boundary to Mars. At 2:01 UT, the plasma properties in the upper ionosphere are already significantly disturbed. The ionospheric upper boundary moves slightly upward. Two kinks are formed near 200 km and 400 km altitude. At the same time, both the induced field and plasma flow velocity are significantly perturbed (Figures 10b2 and 10c2). Similar to Event 1, at 1000 km, the antisunward plasma velocity increases by more than a factor of 3. The vertical profile of the induced magnetic field also changes, forming a broad peak at high altitude and a narrow peak at around 200 km and a dip around 350 km. The magnitude of the induced field is more than doubled from 45 nT to 94 nT at around 200 km altitude. These profiles demonstrate that the ionosphere responds to the solar wind velocity variation almost instantaneously. Again, the kinks in electron density disappear very shortly as shown in Figure 10a3. This panel also shows that the density of O^+ is enhanced at 2:02 UT between 300 km and

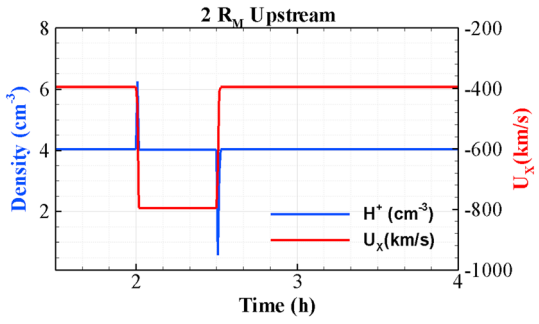

Figure 9. Variation of the density and velocity of the plasma at 2 R_M upstream along the subsolar line.

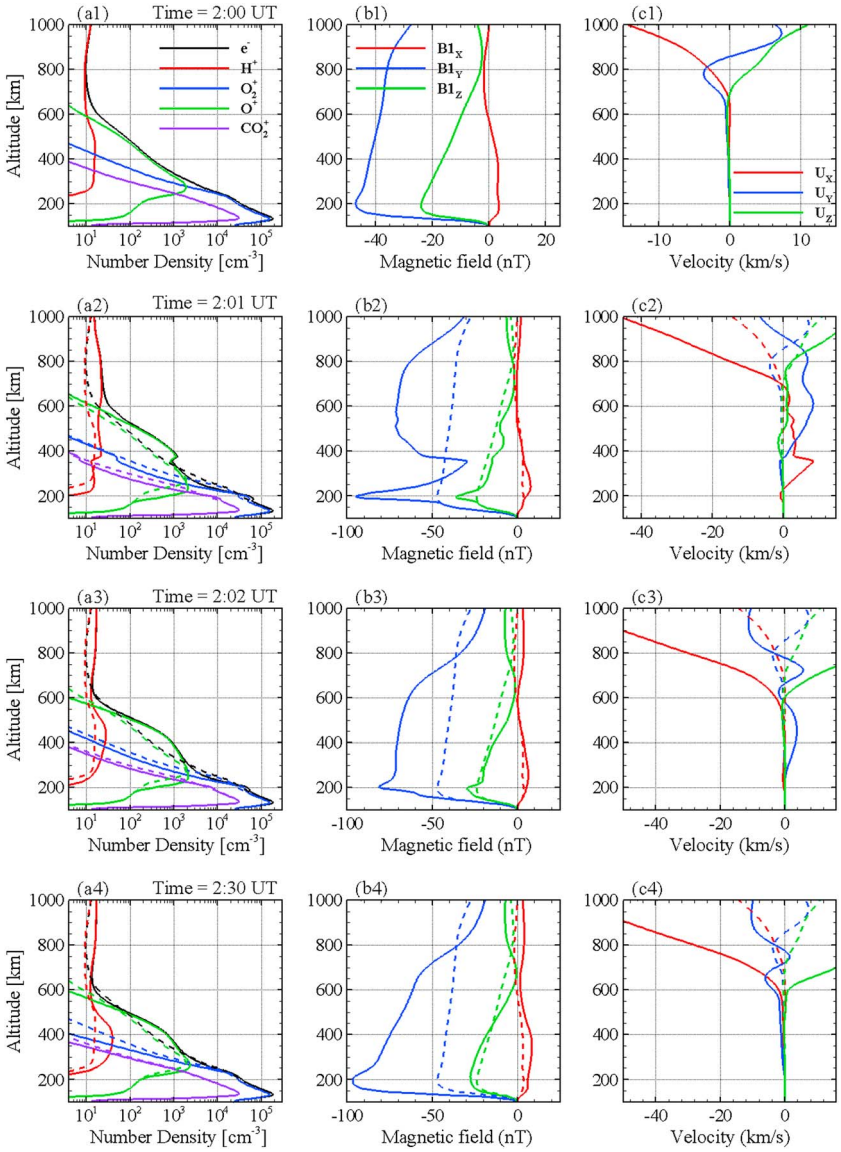

Figure 10. Snapshots of various plasma properties along the subsolar line at different simulation times. (a1–a8) Altitude profiles of number densities of different ion species and electrons, and (b1–b8 and c1–c8) altitude profiles of magnetic field and velocity components, respectively.

500 km altitude, similar to Event 1, which is mainly due to the enhanced compression of the ionosphere. At 2:02 UT, the induced field at very low altitude decreased slightly. The flow velocity is dominated by the downward component above 600 km, but becomes dominated in positive *Y* direction below 600 km altitude. Afterward, the ionospheric density profiles together with the magnetic field and flow velocity all slowly vary to reach a new quasi steady state.

At 2:31 UT, only 1 min after the solar wind pressure/velocity drop at the outer boundary, the plasma flow has already changed its direction to move upward with a speed of 20 km/s near 1000 km (Figure 10c5). At the same time, the topside ionosphere extends to about 750 km altitude (Figure 10a5), while the induced magnetic field also decreases dramatically above 250 km (Figure 10b5). The ionosphere along the subsolar line keeps extending to around 900 km at 2:32 UT. A broad dip of the magnetic field is also found in Figure 10b6, similar to the magnetic field signature in Event 1 at a similar time. The broad dip shrinks quickly and disappears at 2:35 UT. After 2:35 UT, the ionosphere again only varies slowly, with the ionosphere top boundary gradually dropping back to its original location. The new quasi steady state is reached at a similar time, as compared with the first event.

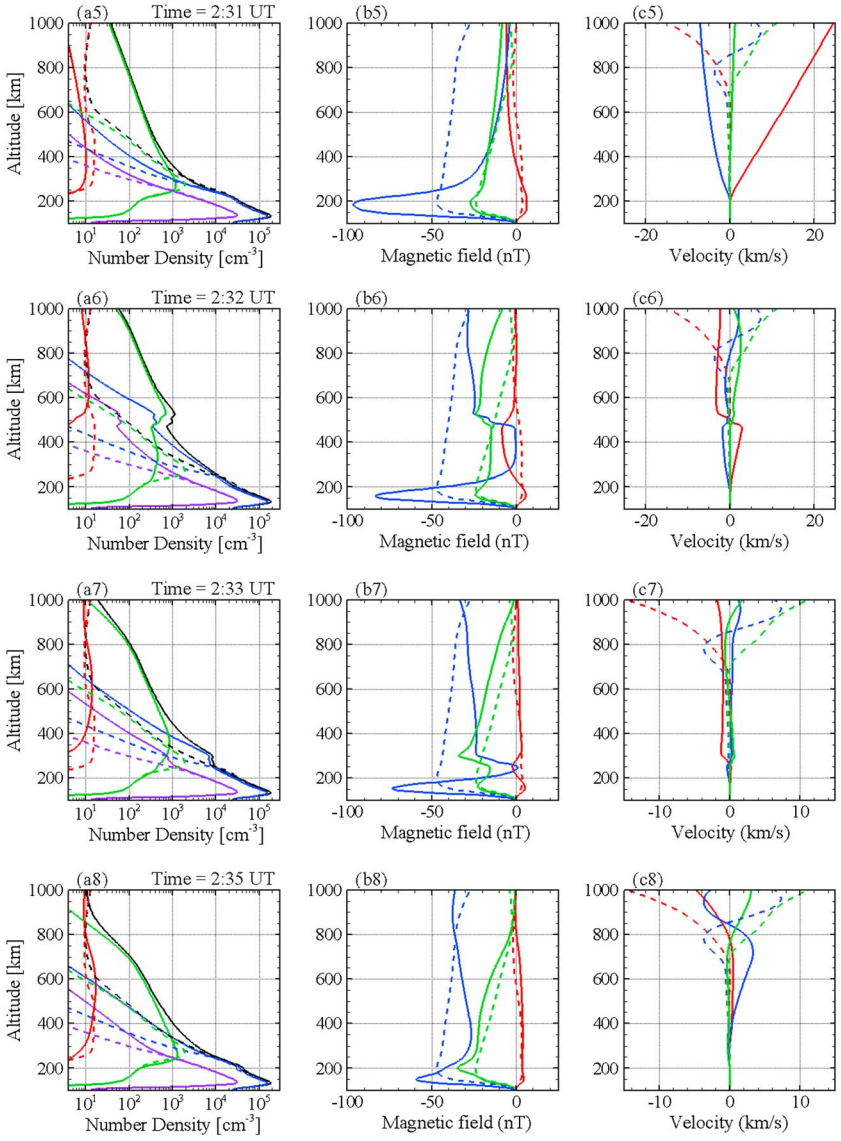

Figure 10. (continued)

Figure 6 (left bottom and right bottom) shows the variation of the interaction boundaries (BS and MPB) for Event 2. Similar to Event 1, we found that the response of the two plasma boundaries to the solar wind pressure enhancement is almost instantaneous (less than 2 min), while it takes a much longer time (~10 min) for the two boundaries to reach their quasi steady state location after the solar wind velocity/dynamic pressure decrease. Also, as compared with the first event, the BS and MPB moves farther away in response to the rarefaction wave that formed around 2:30 UT for Event 2.

Figure 7 (bottom) shows variations of the ionosphere top boundary locations in the *XY* plane for Event 2. The variation is generally similar to the density enhancement event presented in the previous section. However, in this events, we see hardly any changes in the ionospheric upper boundary during the compression phase (at 2:02 UT and 2:30 UT), even though the shape of the electron profiles are significantly altered (as shown in Figure 10). This indicates that density-associated pressure enhancement is more efficient at compression of the ionosphere. Another remarkable difference is that at 2:32, during the expansion phase, the ionosphere reaches 1050 km altitude near 15 LT, much higher than the 800 km altitude during the density enhancement event. Similar to Event 1, the ionosphere top boundary is still not returned to its equilibrium state 30 min after the solar wind back to the quiet condition.

The variation of the ion escape fluxes for Event 2 is shown by dashed lines in Figure 8. The escape fluxes of this event have a similar trend as compared with that of Event 1 in general. The fluxes are slightly larger than that of Event 1 for the two heavy ions (O_2^+ and CO_2^+) during the whole perturbation period and also for O^+, but only after 2:30 UT. For both events, the pressure is enhanced by a factor of 4 for 30 min. The results indicate that velocity-associated pressure enhancement is more efficient in removing the heavy ions from the planet. The O^+ flux is actually slightly smaller than that of Event 1 during the compression phase between 2:00 UT and 2:30 UT. At 2:30 UT, the O^+ flux reaches to 1.23×10^{25}/s, about 2.7 times the quiet time flux value. This is smaller than the escape rates for Event 1 because the solar wind density increase also increases charge exchange reaction rates between proton and oxygen atoms and contributes to an additional loss of O^+. Also worth noting is that there are peaks or dips near 2:00 UT and 2:30 UT, associated with the shock and expansion wave that formed near these times. Similar to Event 1, we find that the initial response of the ionosphere to those perturbations in the solar wind is almost instantaneous; on the other hand, the ionosphere system needs quite a long time to reach a full recovery.

4. Summary

The ionospheric structure at Mars and total ion escape rates depend strongly on the solar wind conditions due to the lack of a strong global internal field. Here we study in detail the ionospheric responses to idealized discontinuities in the solar wind using a 3-D multispecies single-fluid MHD model. This model calculates the densities of the solar wind protons and all the major ion species in the Martian ionosphere, as well as the plasma bulk velocities and energies. The Mars-solar wind interaction is self-consistently calculated in the model by including the effects of the crustal magnetic field, ion-neutral collisions, and major chemical reactions. The radial resolution used in the calculation is as fine as 5 km in the Martian ionosphere to reproduce its response to the solar wind variations.

As shown in both the solar wind density enhancement and velocity enhancement events, the upper ionosphere responds almost instantaneously to the change in the solar wind. However, it takes significant time for the system to adjust to the new solar wind conditions to reach a new quasi-equilibrium. The recovery time scale in both events is more than 1 h. Of course, the time needed for the system to relax from an arbitrary event could vary from event to event. Generally, we expect that more time is needed if the solar wind condition is more disturbed or if the disturbance lasts longer. The time variation flux plots presented in the paper provide a useful guideline for future statistical studies of the solar wind-induced escape fluxes. This suggests that, for future statistical studies, it is necessary to exclude the contamination of ion escape during transient space weather events in order to examine the direct relationship between escape fluxes and solar wind conditions. However, this may not cause much difference when estimating the escape flux relation to the solar wind condition for long-time events such as CMEs and CIRs, which usually last for days.

We also find that, in general, a density-associated pressure enhancement event is quite similar to a velocity-associated pressure enhancement event. The results of both events show significant compression of the magnetosphere and large variation of density profiles, but only limited change of the ionospheric top boundary locations during the solar wind pressure enhancement phase. While during pressure decreasing phase, there is some expansion of the magnetosphere but drastic extension of the ionosphere. The results also suggest that a velocity-associated pressure enhancement is more efficient in removing the heavy ions from the planet; while density associate pressure enhancement is more efficient in removing the O^+ from the planet.

Even though the two events presented here are ideal and thus cannot be directly compared with observations, we noticed that many of the observed features are similar to what has been reproduced by the model during these simplified events. This explains why the upper ionosphere is highly variable. It is also found that the integrated escape fluxes do not directly correlate with the simultaneous solar wind dynamic pressure. Rather, they also depend on earlier solar wind conditions. It can take a few hours for the ionosphere system to reach a new quasi-equilibrium state. However, the simulations presented in the paper neglected the rotation of the planet and the associated crustal field effects. A solar wind monitor at Mars is needed to further understand the shape and structure of the topside ionosphere and their relation with the solar wind variations. This will soon be possible with the upcoming Mars Atmosphere and Volatile Evolution mission and probable coordinated observations with the Mars Express mission.

Acknowledgments
The work was supported by NASA grant NNX11AN38G and NSF grant AST-0908472. Resources supporting this work were provided by the NASA High-End Computing (HEC) Program through the NASA Advanced Supercomputing (NAS) Division at Ames Research Center.

Masaki Fujimoto thanks Hermann Opgenoorth and an anonymous reviewer for their assistance in evaluating this paper.

References

Acuna, M. H., et al. (1998), Magnetic field and plasma observations at Mars: Initial results of the Mars Global Surveyor mission, *Science*, *279*, 1676–1680.

Arkani-Hamed, J. (2001), A 50-degree spherical harmonic model of the magnetic field of Mars, *J. Geophys. Res.*, *106*, 23,197–23,208.

Boesswetter, A., H. Lammer, Y. Kulikov, U. Motschmann, and S. Simon (2010), Non-thermal water loss of the early Mars: 3D multi-ion hybrid simulations, *Planet. Space Sci.*, *58*(14-15), 2031.

Brecht, S. H., and S. A. Ledvina (2012), Control of ion loss from Mars during solar minimum, *Earth Planets Space*, *64*, 165–178.

Dieval, C., et al. (2012), A case study of proton precipitation at Mars: Mars Express observations and hybrid simulations, *J. Geophys. Res.*, *117*, A06222, doi:10.1029/2012JA017537.

Dubinin, E., M. Fraenz, J. Woch, F. Duru, D. Gurnett, R. Modolo, S. Barabash, and R. Lundin (2009), Ionospheric storms on Mars: Impact of the corotating interaction region, *Geophys. Res. Lett.*, *36*, L01105, doi:10.1029/2008GL036559.

Edberg, N. J. T., H. Nilsson, A. O. Williams, M. Lester, S. E. Milan, S. W. H. Cowley, M. Fränz, S. Barabash, and Y. Futaana (2010), Pumping out the atmosphere of Mars through solar wind pressure pulses, *Geophys. Res. Lett.*, *37*, L03107, doi:10.1029/2009GL041814.

Fang, X., M. W. Liemohn, A. F. Nagy, Y. Ma, D. L. De Zeeuw, J. U. Kozyra, and T. H. Zurbuchen (2008), Pickup oxygen ion velocity space and spatial distribution around Mars, *J. Geophys. Res.*, *113*, A02210, doi:10.1029/2007JA012736.

Fang, X., M. W. Liemohn, A. F. Nagy, J. Luhmann, and Y. Ma (2010a), On the effect of the Martian crustal magnetic field on atmospheric erosion, *Icarus*, *206*, 130–138, doi:10.1016/j.icarus.2009.01.012.

Fang, X., M. W. Liemohn, A. F. Nagy, J. G. Luhmann, and Y. Ma (2010b), Escape probability of Martian atmospheric ions: Controlling effects of the electromagnetic fields, *J. Geophys. Res.*, *115*, A04308, doi:10.1029/2009JA014929.

Fang, X., S. W. Bougher, R. E. Johnson, J. G. Luhmann, Y. Ma, Y.-C. Wang, and M. W. Liemohn (2013), The importance of pickup oxygen ion precipitation to the Mars upper atmosphere under extreme solar wind conditions, *Geophys. Res. Lett.*, *40*, 1922–1927, doi:10.1002/grl.50415.

Futaana, Y., et al. (2008), Mars Express and Venus Express multi-point observations of geoeffective solar flare events in December 2006, *Planet. Space Sci.*, *56*, 873–880, doi:10.1016/j.pss.2007.10.014.

Harnett, E. M. (2009), High-resolution multifluid simulations of flux ropes in the Martian magnetosphere, *J. Geophys. Res.*, *114*, A01208, doi:10.1029/2008JA013648.

Harnett, E. M., and R. M. Winglee (2006), Three-dimensional multifluid simulations of ionospheric loss at Mars from nominal solar wind conditions to magnetic cloud events, *J. Geophys. Res.*, *111*, A09213, doi:10.1029/2006JA011724.

Harnett, E. M., and R. M. Winglee (2007), High resolution multi-fluid simulations of the plasma environment near the Martian magnetic anomalies, *J. Geophys. Res.*, *112*, A05207, doi:10.1029/2006JA012001.

Kallio, E., K. Liu, R. Jarvinen, V. Pohjola, and P. Janhunen (2009), Oxygen ion escape at Mars in a hybrid model: High energy and low energy ions, *Icarus*, *206*(1), 152–163.

Kallio, E., K. Liu, R. Jarvinen, V. Pohjola, and P. Janhunen (2010), Oxygen ion escape at Mars in a hybrid model: High energy and low energy ions, *Icarus*, *206*(1), 152–163, doi:10.1016/j.icarus.2009.05.015.

Lundin, R., S. Barabash, A. Fedorov, M. Holmström, H. Nilsson, J.-A. Sauvaud, and M. Yamauchi (2008), Solar forcing and planetary ion escape from Mars, *Geophys. Res. Lett.*, *35*, L09203, doi:10.1029/2007GL032884.

Ma, Y., A. F. Nagy, K. C. Hansen, D. L. DeZeeuw, and T. I. Gombosi (2002), Three-dimensional multispecies MHD studies of the solar wind interaction with Mars in the presence of crustal fields, *J. Geophys. Res.*, *107*(A10), 1282, doi:10.1029/2002JA009293.

Ma, Y., A. F. Nagy, I. V. Sokolov, and K. C. Hansen (2004), Three-dimensional, multispecies, high spatial resolution MHD studies of the solar wind interaction with Mars, *J. Geophys. Res.*, *109*, A07211, doi:10.1029/2003JA010367.

Ma, Y.-J., and A. F. Nagy (2007), Ion escape fluxes from Mars, *Geophys. Res. Lett.*, *34*, L08201, doi:10.1029/2006GL029208.

Modolo, R., G. M. Chanteur, E. Dubinin, and A. P. Matthews (2006), Simulated solar wind plasma interaction with the Martian exosphere: Influence of the solar EUV flux on the bow shock and the magnetic pile-up boundary, *Ann. Geophys.*, *24*, 3403–3410.

Najib, D., A. F. Nagy, G. Tóth, and Y. Ma (2011), Three-dimensional, multifluid, high spatial resolution MHD model studies of the solar wind interaction with Mars, *J. Geophys. Res.*, *116*, A05204, doi:10.1029/2010JA016272.

Nilsson, H., E. Carlsson, D. A. Brain, M. Yamauchi, M. Holmstrom, S. Barabash, R. Lundin, and Y. Futaana (2010), Ion escape from Mars as a function of solar wind conditions: A statistical study, *Icarus*, *206*(1), 40–49, doi:10.1016/j.icarus.2009.03.006.

Opgenoorth, H. J., D. J. Andrews, M. Fränz, M. Lester, N. J. T. Edberg, D. Morgan, F. Duru, O. Witasse, and A. O. Williams (2013), Mars ionospheric response to solar wind variability, *J. Geophys. Res. Space Physics*, *118*, 6558–6587, doi:10.1002/jgra.50537.

Powell, K. G., P. L. Roe, T. J. Linde, T. I. Gombosi, and D. L. DeZeeuw (1999), A solution-adaptive upwind scheme for ideal magnetohydrodynamics, *J. Comput. Phys.*, *154*, 284–309.

Schunk, R. W., and A. F. Nagy (2009), *Ionospheres*, 2nd ed., Cambridge Univ. Press, New York.

Terada, N., Y. N. Kulikov, H. Lammer, H. I. M. Lichtenegger, T. Tanaka, H. Shinagawa, and T. Zhang (2009), Atmosphere and water loss from early Mars under extreme solar wind and extreme ultraviolet conditions, *Astrobiology*, *9*(1), 55–70, doi:10.1089/ast.2008.0250.

Toth, G., et al. (2012), Adaptive numerical algorithms in space weather modeling, *J. Comput. Phys.*, *231*(3), 870–903, doi:10.1016/j.jcp.2011.02.006.

Vignes, D., et al. (2000), The solar wind interaction with Mars: Locations and shapes of the bow shock and the magnetic pile-up boundary from the observations of the MAG/ER Experiment onboard Mars Global Surveyor, *Geophys. Res. Lett.*, *27*(1), 49–52, doi:10.1029/1999GL010703.

Withers, P., et al. (2012), A clear view of the multifaceted dayside ionosphere of Mars, *Geophys. Res. Lett.*, *39*, L18202, doi:10.1029/2012GL053193.